

South Dakota State University

Open PRAIRIE: Open Public Research Access Institutional Repository and Information Exchange

Electronic Theses and Dissertations

2022

Superhalogen-Based Li-Rich Anti-Perovskite Superionic Conductors

Md Mominul Islam

South Dakota State University, mdmominul.islam@jacks.sdstate.edu

Follow this and additional works at: <https://openprairie.sdstate.edu/etd2>



Part of the [Power and Energy Commons](#)

Recommended Citation

Islam, Md Mominul, "Superhalogen-Based Li-Rich Anti-Perovskite Superionic Conductors" (2022). *Electronic Theses and Dissertations*. 445. <https://openprairie.sdstate.edu/etd2/445>

This Thesis - Open Access is brought to you for free and open access by Open PRAIRIE: Open Public Research Access Institutional Repository and Information Exchange. It has been accepted for inclusion in Electronic Theses and Dissertations by an authorized administrator of Open PRAIRIE: Open Public Research Access Institutional Repository and Information Exchange. For more information, please contact michael.biondo@sdstate.edu.

SUPERHALOGEN-BASED LI-RICH ANTI-PEROVSKITE SUPERIONIC CONDUCTORS

BY

MD MOMINUL ISLAM

A thesis submitted in partial fulfillment of the requirements for the

Master of Science

Major in Electrical Engineering

South Dakota State University

2022

THESIS ACCEPTANCE PAGE

Md Mominul Islam

This thesis is approved as a creditable and independent investigation by a candidate for the master's degree and is acceptable for meeting the thesis requirements for this degree.

Acceptance of this does not imply that the conclusions reached by the candidate are necessarily the conclusions of the major department.

Yue Zhou
Advisor

Date

George Hamer

Nicole Lounsbery, PhD
Director, Graduate School

Date

ACKNOWLEDGEMENTS

First, I would like to express my gratitude to Dr. Yue Zhou for providing me an opportunity to work as a graduate research and teaching assistant at South Dakota State University. Dr. Zhou's dedication and passion for research motivated me in many aspects. I appreciate his guidance and encouragement throughout the course of my research work.

This thesis work was supported by was supported by NASA (80NSSC21M0147). We also acknowledge the support from South Dakota Governor's Research Center and SDBoR Competitive Grant Program.

I would like to thank Abdullah-Al-Maruf for completing the theoretical portion which is one of the core components in my research.

I would also like to thank Associate Prof. Parashu Kharel for agreeing to serve on my oral defense and giving me his valuable time and feedback for my thesis work.

I felt blessed to work with many of the wonderful people in the group. Among many others, I would like to thank Dr. Rajesh Pathak, Dr. Ke Chen, Jyotshna Pokharel, Buddhi Sagar Lamsal, Wei He, and Tahmid Alam for their generous help.

I would like to thank my parents Md Monzurul Islam Sarker and Momtaz Shanaz, for their love and support, despite being thousands of miles away. Lastly, special thanks goes to my wife Nasrin Sultana Islam for her constant support, love, and encouragement.

TABLE OF CONTENTS

ABSTRACT.....	v
CHAPTER 1 - INTRODUCTION.....	1
1.1 BACKGROUND.....	1
1.2 PREVIOUS WORK	3
1.3 MOTIVATION.....	5
1.4 OBJECTIVE	6
CHAPTER 2 - THEORY	8
2.1 COMPONENTS AND WORKING PRINCIPLE OF LI-ION BATTERIES	8
2.2 BATTERY PERFORMANCE EVALUATION METRICS	9
2.3 MATERIAL CHARACTERIZATIONS.....	10
2.4 ELECTROCHEMICAL CHARACTERIZATIONS.....	12
CHAPTER 3 - EXPERIMENTAL PROCEDURES	15
3.1 DFT CALCULATION METHOD	15
3.2 CONVERGENCE PARAMETER FOR DFT	1
3.3 BANDGAP.....	2
3.4 MATERIALS SYNTHESIS.....	4
3.5 MATERIALS CHARACTERIZATION.....	5
3.6 ELECTROCHEMICAL CHARACTERIZATIONS.....	7
CHAPTER 4 - RESULTS	10
4.1 ELASTIC AND ELECTRONIC PROPERTIES	10
4.2 IONIC CONDUCTIVITY MEASUREMENT	12
4.3 XRD PEAKS COMPARISON.....	13
4.4 SURFACE TOPOLOGY	14
4.5 IMPEDANCE SPECTROSCOPY.....	15
4.6 SYMMETRICAL CELL PERFORMANCE	16
4.7 FULL CELL PERFORMANCE	17
CHAPTER 5 - DISCUSSION	19
5.1 CONCLUSION.....	19
5.2 FUTURE WORK	20
LITERATURE CITED	21

ABSTRACT

SUPERHALOGEN-BASED LI-RICH ANTI-PEROVSKITE SUPERIONIC CONDUCTORS

MD MOMINUL ISLAM

2022

Solid-state batteries are being widely explored to meet next-generation energy storage demand with a great potentiality of achieving high energy and power densities at All-solid-state Lithium-ion batteries (LIBs). In recent years, electronically inverted lithium-rich anti-perovskite (LiRAP) solid electrolytes with the formula Li_3OX , where X is a halogen or mixture of halogens have appeared as a prospective alternative of the commercially available flammable and corrosive organic liquid electrolytes because of their high ionic conductivity, structural variety, and wide electrochemical window. Here, For the first time, we have successfully formulated and synthesized a completely new class of super halogen based double anti-perovskite named $\text{Li}_6\text{OS}(\text{BH}_4)_2$ using thin film methodology. As the earliest step, using density functional theory (DFT), the formation energy approach has been employed to determine the thermodynamically stability of $\text{Li}_6\text{OS}(\text{BH}_4)_2$. The objective of this research is to find stable solid electrolyte that would be compatible for new lithium-ion battery. Experimental characterization supported the theoretical prediction that super halogen substitution of X (X= Cl, Br etc.) leads to stabilization of the double anti-perovskite structure with a low activation barrier for Li^+ diffusion.

We have found that the novel anti-perovskite provides a systematically larger band gap that can serve to inhibit bulk conductivity, and large spin–orbit coupling for band inversion. The performance of the symmetrical Li/ Li₆OS(BH₄)₂/Li cell was steady and lasted around 3000 hours without a short circuit. At 0.02 C, the steady specific capacity of the solid-state LiFePO₄/ Li₆OS(BH₄)₂ /Li battery is 132 mAhg⁻¹. The advantages and disadvantages of designing and using the reported material in cutting-edge solid-state batteries are also explored. This new class of super-halogen based double anti-perovskite is a promising way to develop the compact solid electrolyte at low temperature for solid-state lithium-ion batteries.

CHAPTER 1 - INTRODUCTION

1.1 Background

Electrochemical energy storage in the form of rechargeable batteries, especially lithium-ion batteries with the highest gravimetric and volumetric energy densities, low-self discharge, longer life cycles at an affordable cost, have become ubiquitous in portable electronics[1] and electric vehicles [2][3]. Notably, Sony Corporation introduced the world's first commercial lithium-ion batteries (LIBs) in 1991 based on $\text{Li}_{1-x}\text{CoO}_2$ cell of Yoshino from the Asahi Kasei Corporation [4][5]. Identical to other electrochemical appliances, batteries are also comprised of an electrolyte that enables the exchange of ions from the anode (negative) to the cathode (positive) during discharge. Li-ions are eliminated from the cathode during charging and move through electrolytes into the anode. Because of the applied electric force, electrons move from cathode to anode through an external circuit [6].

Nonetheless, the commercial lithium batteries with carbonaceous materials [7] (graphite, carbon nanotubes, nanofibers, and graphene) as anodes [8], transition metal oxides (LiTi_2O_4 , LiV_2O_4 , and LiMn_2O_4) as cathodes [9] as well as ethylene carbonate-based electrolytes [10] can produce an energy density of $100\text{-}265 \text{ Whkg}^{-1}$ [11] that limits the further deployment of LIBs on emerging applications in electric vehicles. Moreover, the usage of graphite anode (theoretical specific capacity of 372 mAhg^{-1} [12]) is one of the significant drawbacks of the lower energy density of the current commercial Li-ion batteries. Therefore, researchers of the modern world are devoted to exploiting novel high-energy-density rechargeable battery systems to meet the ever-growing energy demand.

The Li-metal, which has the highest theoretical capacity (3860 mAhg^{-1}), lowest electrochemical potential (-3.04 V versus H/H^+), and the lowest density (0.59 gcm^{-3}), has been widely investigated [13] as the optimal choice to replace the graphite anode. However, due to the formation of Li dendrites [14], the low Coulombic efficiency after long-term charging and discharging [11], and the continual reaction of Li-metal with flammable organic liquid electrolytes, the use of the Li-metal anode in organic liquid electrolytes is impeded [15].

To properly address the safety concerns, highly flammable organic liquid electrolytes should be replaced with new solid electrolytes (SEs), which have better electrochemical stability [16]. The major benefit of using SEs is the increased safety [1], which is analyzed further to find other beneficial features. Using SEs instead of liquid electrolytes will solve the drawbacks of liquid electrolytes and open opportunities for new battery chemistries to be devised. With an ability to stabilize the solid electrolyte interphase (SEI), a new era of all-solid-state Li-metal batteries (ASS-LMBs) [14] with SEs has been introduced. Additionally, the use of SEs as separator limits the formation of Li dendrites, which addresses the shuttle effect of poly sulfides in Li-S batteries and electrode erosion in Li-O₂ battery technologies.

As a core component of ASS-LMBs, the SEs are generally required to possess stable performance ability, no aging effects like mechanical degradation in Lithium batteries, stable battery operation at a wide temperature range (like -50 to $200 \text{ }^\circ\text{C}$ or higher), and high ionic conductivity [15][17][18]. To date, various types of SEs have been introduced, including Oxides, sulfides, hydrides, halides, and polymers with room-temperature ionic conductivities up to $10^{-4}\sim 10^{-2} \text{ Scm}^{-1}$ [14]. Although much progress has

been made in improving the properties mentioned above, each SE has its features [15]. Therefore, it is hard to fabricate and obtain a perfect SSE with all desired properties.

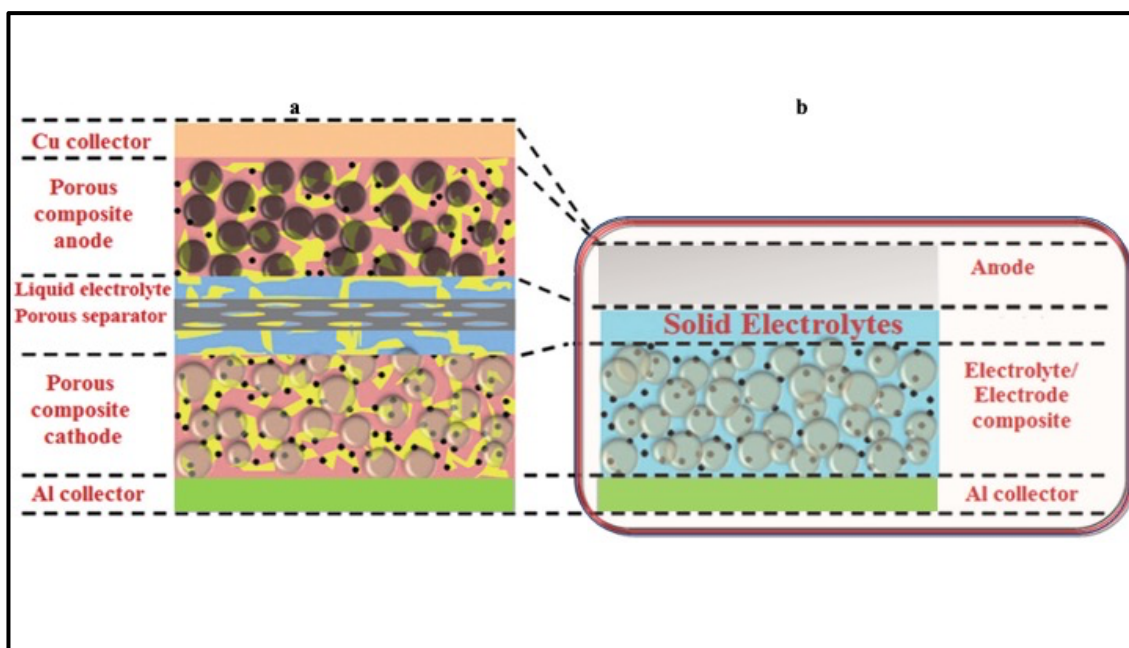


Figure 1: (a-b) Schematic demonstration of Li-ion battery using liquid electrolyte and solid-state electrolyte [19]

1.2 Previous Work

In recent years, different types of SEs have been widely investigated. Solid electrolytes can be categorized into Oxide type, sulfide type, hydride type, halide type, thin-film type, and polymer-based materials.

The first major milestone in developing SSE was reached through achieving superb ionic conductivity, ultra-fast transportation of Li^+ ions along with lower crystallinity in the LGPS family of materials, tetragonal samples like $\text{Li}_{10}\text{GeP}_2\text{S}_{12}$, Li_7GePS_8 , and $\text{Li}_{9.54}\text{Si}_{1.74}\text{P}_{1.44}\text{S}_{11.7}\text{C}_{10.3}$.

Reported coulombic efficiency(η) for the $\text{Li}_{9.6}\text{P}_3\text{S}_{12}$, $\text{Li}_{10}\text{GeP}_2\text{S}_{12}$ and $\text{Li}_{9.54}\text{Si}_{1.74}\text{P}_{1.44}\text{S}_{11.7}\text{C}_{10.3}$ cells was 90%, 61% and 39% [20] [21][22]. However, the LGPS families are not electrochemically compatible with the Li anode due to the formation of poor ionic and electric conductors such as Li_2S at the interface [22].

Among the oxide-based SEs, NASICON-type [23][24] materials were introduced after the discovery of $\text{Na}_{1+x}\text{Zr}_2\text{Si}_x\text{P}_{3-x}\text{O}_{12}$ compound with the general formula $\text{AM}_2(\text{PO}_4)_3$ where A site filled by Group IA metals like Li, Na or K and M site with Ge, Zr or Ti. Although NASICON-type compounds such as $\text{Li}_{1+x}\text{Al}_x\text{Ge}_2\text{P}_3(\text{PO}_3)_4$ (LAGP) had superior ion conductivity and moisture stability, Linchun et al claimed that LAGP was unstable with Li metal. LISICON-type [25] solid electrolytes (SEs) like $\text{Li}_{14}\text{ZnGe}_4\text{O}_{16}$ were originally described by Hong et al in 1978, and Robertson et al [26] in 1997 introduced $\text{Li}_{14}\text{ZnGe}_4\text{O}_{16}$, although both had lower ionic conductivity (10^{-7} Scm^{-1} at ambient temperature). Thangadurai and Weppner et al [27] later developed $\text{Li}_{14}\text{ZnGe}_4\text{O}_{16}$, which is extremely reactive with Li metal and atmospheric CO_2 and has a decreasing conductivity over time. Thangadurai and Weppner (2005a) et al developed Garnet-type lithium single ion conductors with a general formula of $\text{Li}_5\text{La}_3\text{M}_2\text{O}_{12}$ (M D Ta, Nb) with a conductivity of ($1.8 \times 10^{-4} \text{ Scm}^{-1}$ at 50°C) after extensive research on SEs. Garnet-type has a low activation energy when the M site in $\text{Li}_5\text{La}_3\text{M}_2\text{O}_{12}$ was partially substituted by Y or In. However, after further investigation, it was discovered that garnets are similarly susceptible to moisture, and their ionic conductivity reduces when Li_2CO_3 forms. The major disadvantages of oxide-based SEs are their non-flexible nature and expensive large-scale production.

Sulfide based oxides were developed in 1986 with the $\text{Li}_2\text{S-SiS}_2$ system. Since then, $\text{Li}_2\text{S-SiS}_2$ type electrolytes have been investigated thoroughly because of their high conductivity, good mechanical strength and mechanical flexibility, and low grain boundary resistance. Due to the polarizable nature of sulfur anion, greater ionic conductivity sulfide-based SSEs (LiPON, garnets, LISICON, LTAP, etc.) have been researched as an alternative to oxide-type SSEs (LiPON, garnets, LISICON, LTAP, etc.). Till today, the highest reported conductivity is $6.9 \times 10^{-4} \text{ Scm}^{-1}$ as the $\text{Li}_2\text{S-SiS}_2$ system was heavily doped with Li_3PO_4 . Later in 2001, a new class of thio-LISICON (LISICON, lithium superionic conductor) was included in the $\text{Li}_2\text{S-SiS}_2$ system [28]. But with time, researchers found out that sulfide-based SEs have low oxidation stability, and they are highly sensitive to moisture.

In recent years, polymer electrolytes were also considered to be a promising alternative to the liquid electrolyte, can be divided into three classes: dry solid polymer electrolytes, gel polymer electrolytes and composite polymer electrolytes. The polymer host, in combination with a lithium salt, acts as a solid solvent in dry solid polymer electrolytes (without any liquid). At room temperature, however, the ionic conductivity of dry polymer systems is quite low.

1.3 Motivation

Need to improve the functionalities of SEs such as (I) ionic conductivity, (II) lower activation energy, (III) large bandgap to hinder electric conduction, (IV) compatible with lithium metal anode, and (V) low-cost fabrication and commercialization process. Additionally, we need to solve the interfacial contact issues of solid electrolyte and lithium

anode. Moreover, we need to reduce to the large grain boundary resistance that exists in current SEs by modifying the fabrication process.

1.4 Objective

The objective of this work is to determine if a new lithium-rich anti-perovskite (LiRAP) family can enhance the ionic conductivity of lithium batteries using solid electrolytes. The following tasks were performed to achieve the goal:

1. Development of new a new family of lithium-rich double anti-perovskite (LiRAP) which will contain a high number of mobile Li-ions in the crystal lattice and has a low energy barrier for ionic transport, using MD simulations and DFT calculations and validating the theoretical approach with practical fabrication.
2. A novel fabrication technique to synthesize a new solid electrolyte which will be compatible with the Li metal anode to achieve better electrochemical battery performance.
3. Develop a novel material by
 - a. Ball milling and thermal annealing process
 - b. Thin-film fabrication using liquid phase synthesis approach
 - c. Use of super halogen instead of traditional halogens
4. Optimize the experimental condition for developing the novel solid electrolyte material including controlling the thickness and solving the interfacial contact issues.
5. Execute the structural and morphological characterization using X-ray diffraction, Raman spectroscopy, and field emission scanning electron microscopy/ energy dispersive spectroscopy (FESEM/EDS).

6. Accomplish the electrochemical characterization using cyclic voltammetry (CV), electrochemical impedance spectroscopy (EIS), symmetrical cell test, and full cell test.

CHAPTER 2 - THEORY

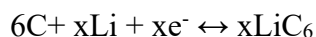
2.1 Components and working principle of Li-ion batteries

In each battery, there is a separator immersed in an electrolyte solution containing dissociated Li salts divides a positive and negative electrode. Negative and positive battery electrodes are composite structures composed of active material particles, a polymeric binder, and a conductive additive. The conductive additive transfers electrons and the porous electrode wets the surface with electrolyte for Li-ion transport. To create appropriate electrical contact between the electrodes, metallic current collectors such as Cu and Al are utilized [29]. The porous separator protects the two electrodes from short-circuiting by acting as an electrically insulating but ionically conducting layer. The cathode gives up its lithium ions to the anode when the battery is charged. During the charging process, the battery stores energy. The lithium ions from the anode migrate back across the electrolyte to the cathode while the battery is discharged, creating the energy that drives the battery. Electrons move in the opposite direction to the ions around the external circuit in both circumstances [30]. During the charge/discharge process, the reaction happens in every electrode. The difference in chemical potential of Li between the two electrodes is the driving force that generates a reaction. The reaction mechanisms are shown in the equations below:

At cathode,



At anode,



2.2

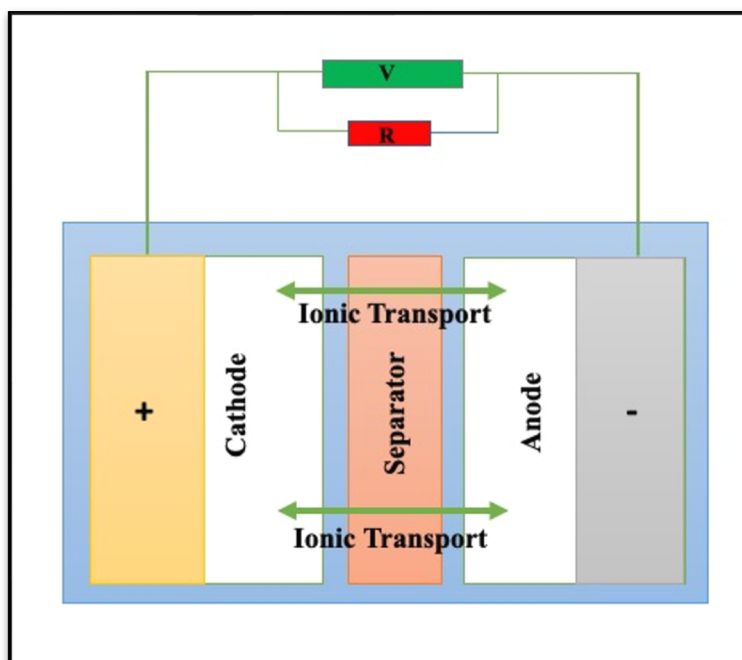


Figure 2: Schematic illustration of the working mechanism in Li-ion battery.

2.2 Battery performance evaluation metrics

The qualities of batteries are determined by the materials used in the electrodes and the size of the batteries. Before designing an energy storage system, it's important to consider the battery's electrical properties, such as current, voltage, and capacity, as well as its thermal characteristics, such as battery performance at various ambient temperatures. This section focuses on understanding the specific capacity, coulombic efficiency (CE) and energy density, cycle life and voltage. The theoretical model and simulation for novel electrolytes of batteries are summarized.

- a) Specific capacity: The capacity is the charge held by applying a specific current (I) for a specific duration (t) (Q). A specific capacity is the amount of charge that can be held per unit mass of electrode materials (SC).
- b) Coulombic efficiency and Cycle life: The ratio of discharge capacity to charge capacity is referred to as Coulombic efficiency (CE). It represents the amount of capacity lost during the cycle. The capacity is reversible if the CE is 100 percent. Side reactions between the anode/cathode and the electrolyte are responsible for CE loss or CE less than 100%. This is an essential parameter that influences the capacity of the battery when the cycle number is increased. Over 100 cycles, a 0.1 percent CE reduction results in a 10% capacity reduction.
- c) Voltage: The difference in chemical potential between the anode and cathode electrode is the main reason to have voltage in battery. The reference voltage value used in Li-battery literature is the electrochemical potential of Li^+/Li .
- d) Energy and power density: The specific energy or gravimetric energy density is the result of integrating the voltage range and specific capacity (Whkg^{-1}). Batteries with high energy density is a good indication that they can store a large amount of energy in a small amount of mass. Whereas batteries with high power density can deliver a large amount of energy in a short time based on its mass.

2.3 Material characterizations

2.3.1 X-ray diffraction spectrum (XRD)

X-ray powder diffraction (XRD) is a quick analytical method that may offer information on unit cell dimensions and is mostly used for phase identification of crystalline materials. The studied material is finely powdered, homogenized, and the bulk

composition is calculated on an average basis. In 1912, Max von Laue observed that crystalline substances operate as three-dimensional diffraction gratings for X-ray wavelengths that are comparable to plane spacing in a crystal lattice. The method of X-ray diffraction is currently widely used to analyze crystal structures and atomic spacing. Constructive interference between monochromatic X-rays and a crystalline sample is the basis of X-ray diffraction [31][32][33].

A cathode ray tube produces the X-rays, which are then filtered to create monochromatic radiation, collimated to focus the beam, and aimed onto the sample. When Bragg's Law ($n\lambda=2d \sin \theta$) is satisfied, constructive interference (and a diffracted ray) results from the interaction of incident rays with the sample. In a crystalline sample, this rule connects the wavelength of electromagnetic radiation to the diffraction angle and lattice spacing. Following that, the diffracted X-rays are detected, processed, and tallied.

Due to the random orientation of the powdered material, scanning the sample across a range of 2 angles should provide all conceivable lattice diffraction directions. Because each mineral has its own set of d-spacings, converting the diffraction peaks to d-spacings enables for mineral identification. This is usually accomplished by comparing d-spacings to established reference patterns. The production of X-rays in an X-ray tube is the basis for all diffraction procedures. The diffracted rays are collected once the X-rays are aimed towards the sample. The angle between the incident and diffracted rays is a critical component of all diffraction. Beyond that, the apparatus for powder and single crystal diffraction differs.

2.3.2 Energy dispersive spectroscopy (EDS)

The technique of energy dispersive spectroscopy (EDS) is mostly employed for qualitative material examination, although it can also provide semi-quantitative results. SEM apparatus is typically paired with an EDS system to allow chemical analysis of features shown in the SEM display. In failure analysis scenarios where spot analysis is critical to reaching a reliable result, simultaneous SEM and EDS analysis is useful. Secondary and backscattered electrons utilized in image formation for morphological analysis, as well as X-rays used for identification and quantification of compounds present at measurable amounts, are among the signals produced by a SEM/EDS system. The detection limit in EDS is determined by the smoothness of the sample surface, the smoother the surface, the lower the detection limit. EDS can detect major and minor elements at concentrations more than 10% wt% (major) and less than 10% wt% (minor) (concentrations between 1 and 10 wt percent) [34][35].

2.4 Electrochemical characterizations

2.4.1 Cyclic voltammetry

The most flexible electroanalytical approach for studying electroactive substances is cyclic voltammetry (CV). CV is widely used in the domains of electrochemistry, inorganic chemistry, organic chemistry, and biochemistry due to its flexibility and simplicity of measurement [36]. The potential of a small, stationary working electrode is altered linearly with time in cyclic voltammetry, starting at a potential where no electrode reaction occurs and progressing to potentials where a solute (the substance being examined) is reduced or oxidized. The direction of the linear sweep is reversed after passing the potential zone in which one or more electrode reactions occur, and the electrode reactions of intermediates and products created during the forward scan are often identified.

The scan (or sweep) rate and total potential traversed govern the time scale of the experiment, which can range from 10^2 - 10^{-5} s to 10 - 10^{-3} s. Quantitative investigations are normally limited to 10 - 10^{-3} s. A supporting electrolyte is present to prevent charged reactants and products from migrating. Because it can give important information regarding redox reactions in a way that is readily produced and analyzed, this basic experiment has become increasingly popular in chemical research.

2.4.2 Electrochemical impedance spectroscopy

EIS (electrochemical impedance spectroscopy) is a useful instrument for analyzing electrochemical processes and charge transfer kinetics. The electrochemical response is measured when an electric potential is applied [37]. EIS is widely employed in a variety of applications, including energy storage, solar, and other electrochemical devices. To understand the internal non-linear electrochemical dynamics, an alternating current (AC) voltage is provided between the electrodes and the function of frequency is documented. The Nyquist plot can be used to analyze the EIS data. The ohmic/ series resistance (R_s), which is the bulk resistance, is shown by the Z-real axis in the Nyquist plot. Charge transfer resistance (R_{ct}) between the two interfaces is determined by the semicircle in the lower frequency range, and the electric double layer capacitance between the interfaces is represented by the constant phase element (CPE) [38]. Warburg impedance (W) is an inclined line in the lower frequency domain that depicts charge diffusion. To match the EIS results, the Randles equivalent circuit can be employed.

2.4.3 Symmetrical cell test

A symmetrical cell test is an electrochemical test that uses the same material as the positive and negative electrodes (for example, a symmetrical cell with Li/Li electrodes on both sides). To comprehend the electrochemical Li plating/stripping cycles, the symmetrical cell can be used. The same Li electrode can be used on both sides of the cell to better understand the Li plating mechanism. To study the Li deposition behavior and long-term voltage versus time profile, plating/stripping can be done at different current densities to produce different capacities. Even though the cell has no voltage Vs Li^+/Li and is therefore ineffective for practical applications, it provides extensive information about the reactions between the electrode materials and the electrolyte.

2.4.4 Half-cell or Full cell test

A half-cell or full cell is a cell having a separate positive and negative electrode that shows the voltage differential. Full cells have anodes other than lithium (such as graphite and tungsten trioxide) and cathodes such lithium cobalt oxide (LCO), Lithium iron phosphate (LFP) and lithium nickel manganese oxide (NMC), whereas half-cells have lithium as anode and any other electrode materials. In lithium metal batteries, a half-cell is sometimes referred to as a full cell.

CHAPTER 3 - EXPERIMENTAL PROCEDURES

3.1 DFT calculation method

First principles electronic calculations were performed in the framework of density functional theory (DFT) as implemented in Quantum Espresso [39].

We used Optimized Norm-Conserving Vanderbilt [40] pseudopotentials and Perdew-Burke-Ernzerhof generalized-gradient approximation (GGA) functional [41] for all DFT calculations. Initially, the total energy and force were fully converged against the cutoff energy, k-point grid, and vacuum along the z-axis in all the slabs before proceeding to any further calculation. In all cases, both the energy and force convergence tolerance were set to 1×10^{-4} Ry. After convergence testing, the cutoff energies for wavefunction and density function were set to 80 Ry and 320. Similarly, A Γ -centered k-point grid by Monkhorst-Pack Method [42] was set to $3 \times 3 \times 3$. All structures are geometrically relaxed until the total force on each ion was reduced below 0.01 eV/Å.

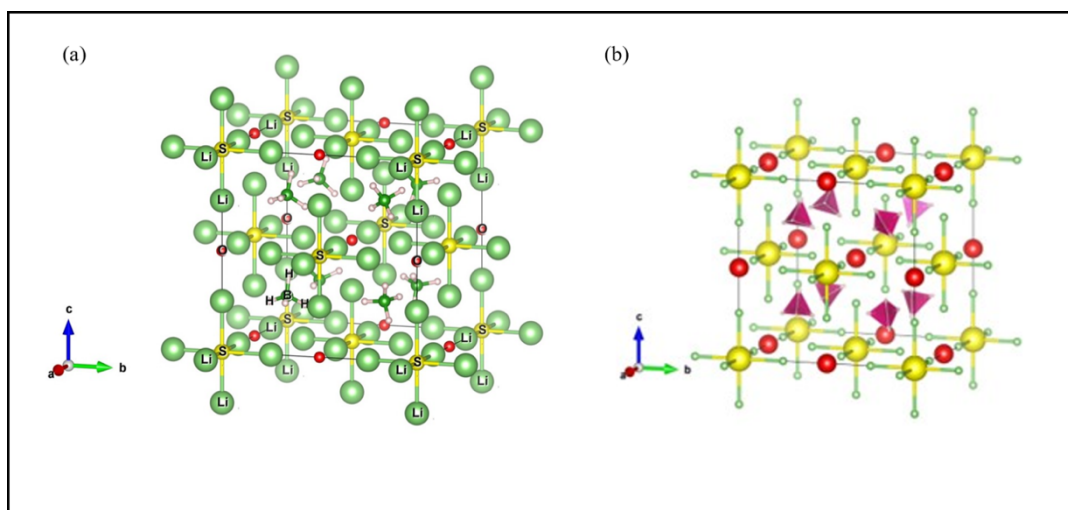


Figure 3: a. *Fm-3m* cubic-face centered crystal structure and ionic structure (b) of $\text{Li}_6\text{OS}(\text{BH}_4)_2$

We employ the PBE0 functional to anticipate more accurate band gap values when calculating electronic energy band topologies. We use a convergence threshold of 10^{-6} eV that is appropriate for electronic self-consistent cycles. To search for the Li^+ diffusion channel in the electrolytes of interest, the climb image nudged elastic band (CI-NEB) approach with the Limited-memory Broyden-Fletcher-Goldfarb-Shanno (LBFGS) optimizer was utilized. After complete structural relaxation, the original and final configurations are achieved. The number of pictures incorporated in the CI-NEB computations is determined by the response coordinates between the original and final configurations. This approach is beneficial for determining the activation barrier as well as pinpointing the bottleneck along the Li^+ carrying channel. A theoretically predicted structure's phonon frequency spectrum is utilized to assess its dynamical stability. The PHONOPY package's super-cell approach is used to do the essential frozen-phonon computations based on harmonic approximation. The phonon computations are performed on supercells of relaxed structures. The amplitude of imaginary frequency must be smaller than 0.3 THz to allow for acceptable numerical mistakes in phonon computations. The formation energy (enthalpy) of each $\text{Li}_a\text{S}_b\text{O}_c(\text{BH}_4)_d$ compound is characterized in terms of the chemical potentials of component elements as,

$$E_f = (E_{comp} - a\mu_{Li} - b\mu_S - c\mu_O - d\mu_{BH_4}) / (a + b + c + d)$$

where E_{comp} is the total energy for the compound and chemical potentials μ_{Li} , μ_{S} , μ_{O} , and μ_{BH_4} are total energy per atom for Li, S, O₂, and BH₄. We used ground state stable structure as reference for each element as listed in the materials project webpage (<https://www.materialsproject.org>)

3.2 Convergence parameter for DFT

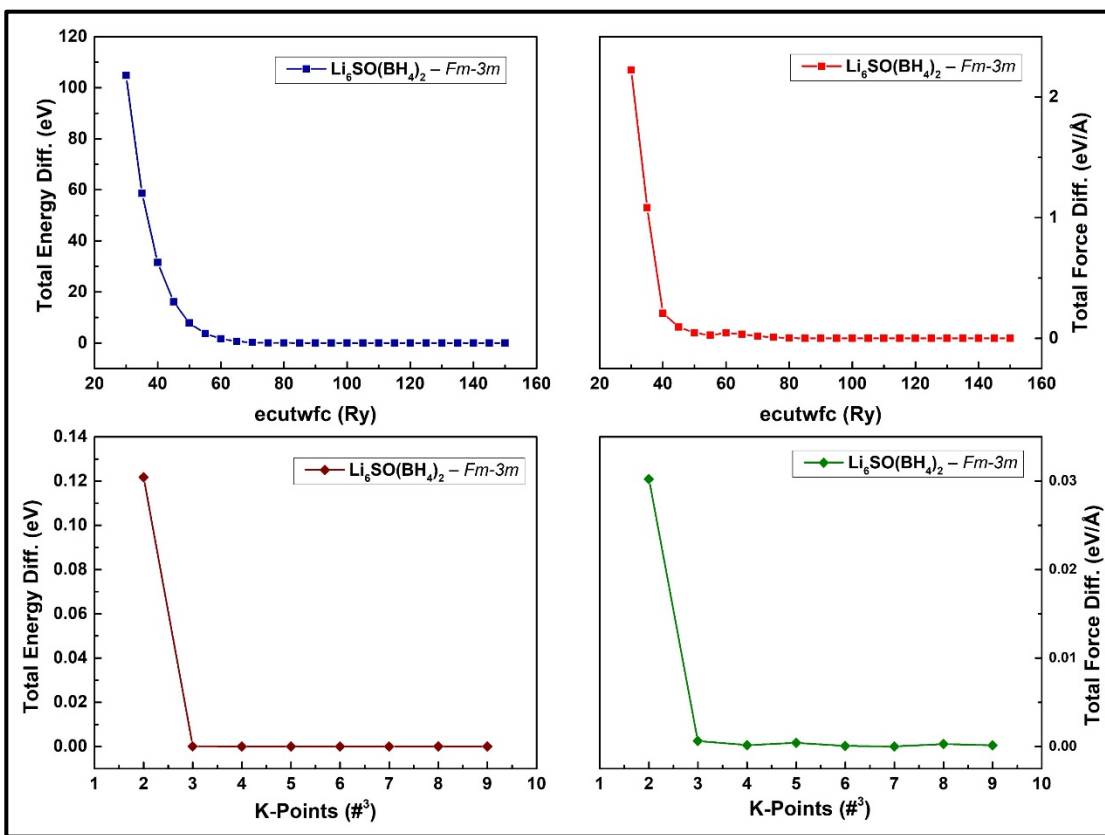


Figure 4: Different convergence parameter for DFT

We have used the formula

$$V_{\text{ext}}(\vec{r}) = + \frac{1}{4\pi\epsilon_0} \sum \frac{eZ_A}{|\vec{r} - \vec{RA}|}$$

For exchange correlation functional: Norm-Conserving Pseudo Potential is used under the framework of Generalized Gradient Approach (GGA) as implemented in Quantum Espresso. After acquiring the surface models, we then discuss the relative stability of the three clean surfaces. The surface energy is an essential element in surface physics and is necessary for simulating a broad range of surface phenomena, particularly surface stability. The surface energy (E_{surf}) may be calculated using the following expression [21]:

$$E_{surf} = \frac{1}{2S} [E_{slab} - N_{slab}E_{bulk}]$$

where E_{slab} is the total energy of a slab model, E_{bulk} represents the total energy of the bulk unit cell, S is the surface area and N_{slab} is the number of bulk unit cells contained in the slab model. We have found the best model approach with an energy cutoff of 80 for wave functions, 320 for density functions and the grid density was chosen to be 3x3x3 on real space.

3.3 Bandgap

As is well recognized, a crucial feature of electrolytes is pure ionic transport with low electrical components. The electrochemical window of a solid electrolyte, which governs the operating voltage range of a battery, is directly dictated by a material's electronic structure [22]. While SSE should be highly conductive to Li^+ ions, it should be insulating for the conduction of electrons to avoid internal discharging. *Figure 10* summarizes the density of states (DOS) for the ionic conductors of interest to this work, using the PBE0 screened hybrid functional for improved accuracy in band structure calculation, by accounting for some non-local effect in the exchange-correlation functional.

Because of the occurrence of very wide forbidden energy gaps between the valence band maximum (VBM) and conduction band minimum (CBM), all materials of concern are insulating to electrons (CBM). In all compounds, electron states of anions dominate both the VBM and CBM. Furthermore, the prohibited gap is demonstrated to be primarily governed by the kind of chalcogen species (O, S), with the gap value being associated to total bonding strength. The prohibited gap in the most firmly bound O-containing material is larger than in the S-based compounds.

$\text{Li}_6\text{SO}(\text{BH}_4)_2$ has shown to be electrically insulator, with band gap 4.0272 eV (>2.2 eV) with PBE exchange correlation functional. While SSE should be highly conductive to Li^+ ions, but it should be insulating for the conduction of electron to avoid internal discharging. High band gap of 4.0272 eV helps to avoid such electrical conduction, even when the Li-battery heats up after long charge-discharge cycles. In contrast to many other known crystalline materials with strong ionic conductivity, the huge band gap suggests that Li_3OCl has exceptional electrochemical stability [43]. It is interesting to note that the electronic states of the conduction band, especially those at high symmetry k-points, are sensitive to the lattice constant.

For the migration of an interstitial Li^+ ion in an anti-perovskite phase, structural relaxation reveals that the presence of an interstitial Li^+ tends to offset a vertex Li^+ of a Li_6S octahedron from its ideal position, forming a dumbbell coordination with the approaching interstitial Li^+ at the vertex point. Emly et al. discovered such a dumbbell formation-decomposition process as the governing mechanism for the movement of interstitial Li^+ ions.

3.4 Materials synthesis

Crystalline materials for $\text{Li}_6\text{OS}(\text{BH}_4)_2$ were synthesized by ball milling and liquid phase approach. The whole process was carried out in a glovebox under Argon atmosphere to isolate the materials from humidity and air. We have developed an efficient synthesis to produce lithium-rich double anti-perovskite. The first step of the synthesis of $\text{Li}_6\text{OS}(\text{BH}_4)_2$ consists of ball milling a mixture of 1 equivalent of Li_2O , 1 equivalent of Li_2S , and 2 equivalent of $\text{Li}(\text{BH}_4)$ for 5 hours. In a typical synthesis, 2.20 gm of Li_2O (>97% purity; powder; Aldrich), 2.20 gm of Li_2S (>99.8% purity; powder; Aldrich), and 4.20 gm of $\text{Li}(\text{BH}_4)$ (>95% purity, powder, Aldrich) are mixed thoroughly by ball milling and then the mixed powder is placed in a tube furnace for 7 hours and heated to 380-400°C under inert gas atmosphere. Moisture is successfully eliminated during heating, and the molten product is swiftly quenched or slowly cooled to room temperature in the tube furnace, resulting in a variety of textures and grain boundary morphologies. The equipment is flushed with a dry inert gas (e.g., Ar) after the synthesis, and the very hygroscopic sample is never exposed to ambient moisture. Continuous heating (380-400 °C at melt) and water removal under high vacuum promote the creation of the $\text{Li}_6\text{OS}(\text{BH}_4)_2$ product:



The reaction in the molten state is simple, and the sample is obtained as a brown, dense, hard polycrystalline mass. Again, the crystalline phase is ball milled for 5 more hours. With successive two ball-milling, we got our final sample ready to be drop cast. We have mixed 0.30 gm of our prepared sample with a solvent 1,2-Dimethoxyethane (DME).

Finally, we have added 0.15 gm Lithium bis(trifluoromethanesulfonyl)imide, often simply referred to as LiTFSI salt, and kept at stirring for about 8 hours. To our knowledge, this is the first publication of the super halogen-based double anti-perovskite, and our ball milling and liquid phase synthesis process are wholly innovative and readily scaled up to make vast amounts of product. Finally, the mixture was drop casted on top of lithium anode.

3.5 Materials characterization

3.5.1 X-ray diffractor

With the use of a sixth generation MiniFlex benchtop X-ray diffractometer, the crystal structure and crystallite size measurement of solid-state electrolytes were examined with Cu-K α radiation ($\lambda = 1.54178$ angstrom). It is the newest addition to the MiniFlex series of benchtop X-ray diffraction analyzers from Rigaku, which began with the introduction of the original MiniFlex XRD system decades ago. MiniFlex X-ray diffraction (XRD) system is versatile enough to perform challenging qualitative and quantitative analyses of a broad range of samples, whether performing research or routine quality control. Cu-k radiation X-rays were utilized to scan the powder samples at a scan rate of 2° per minute across a range of 10° to 90° (2 degrees per minute). Moisture-sensitive anti-perovskite samples were covered with Kapton tape (1 =25 m) before being subjected to XRD examination. The XRD spectrum simulation was carried out with the help of the VESTA 3 software [17]. The X-ray is generated when the applied tube voltage and the current reached 40 KV and 44 mA. Figure 6 shows the picture available XRD setup in the lab at SDSU.



Figure 5: Picture showing the X-ray diffractometer located in the Lab at SDSU.

3.5.2 Scanning electron microscopy and energy dispersive spectroscopy

A Hitachi S-4300 N SEM was used for scanning electron microscopy (SEM) and energy-dispersive X-ray spectroscopy (EDS) characterization. Hitachi S-3400N SEM and Hitachi S-4700N FESEM were used to create SEM pictures, EDS, and elemental mapping. The cross-sectional SEM images and the surface topography were measured. The sensitive samples, such as Li and modified Li, were transported in a closed vial from the glove box

to the SEM chamber. The semiconducting samples were gold-sputtered with the aid of CRC-sputtering utilizing a Hitachi S-4300 N SEM. Depending on the kind of sample, different accelerating voltages were used to scan high resolution and low-resolution SEM pictures. The elemental mapping and EDS spectra were recorded using the Aztec program (Oxford Instruments). scanning electron microscope (SEM) imaging was carried out in a nitrogen environment utilizing a Supra 40VP field emission scanning microscope (Zeiss). The secondary electron collector (SE2) was employed as a detector, with a working distance of 5.0 mm between the secondary electron collector and the target. SEM may be used to study the atomic/weight percentage and elemental distribution. Figure 9 shows the picture of Hitachi S-3400N SEM and Hitachi S-4700N FESEM available in the cleanroom of SDSU.

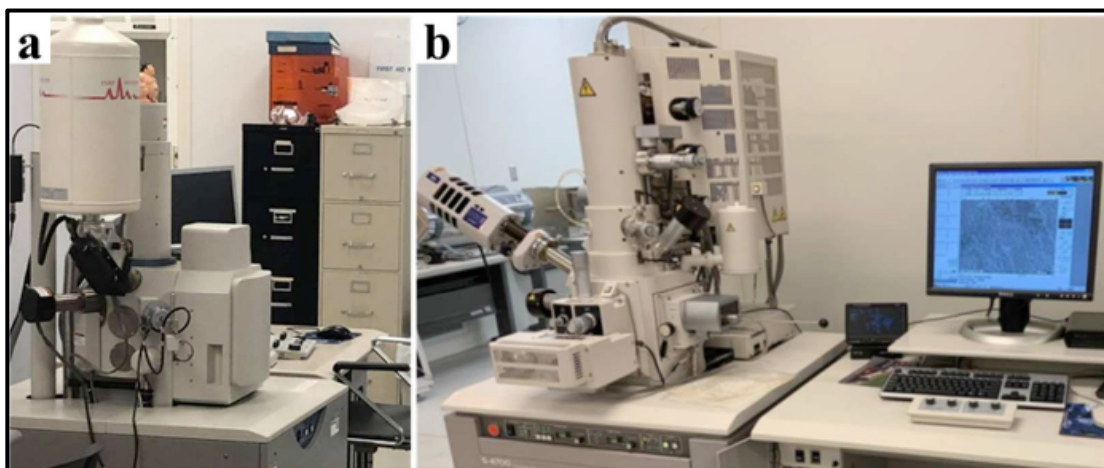


Figure 6: Picture of a Hitachi S-3400N SEM EM and b Hitachi S-4700N FESEM located in the cleanroom at SDSU.

3.6 Electrochemical characterizations

Inside an argon-filled glove box (moisture and O₂ levels 1 ppm), the coin type CR-2032 Li-ion cell was produced using lithium metal as the counter and reference electrode

and LFP as the working electrode. As a separator, a novel double anti-perovskite with a film thickness of 200 μm was utilized.

3.6.1 Cyclic voltammetry and electrochemical impedance spectroscopy

An electrochemical workstation (Ametek VERSASTAT3-200 and EC Lab potentiostat) was used to perform cyclic voltammetry (CV). Over linear sweep voltammetry, the CV was measured in various potential ranges for several cycles in the range 0.1 to 3 V and in a single cycle from -0.2 V to 0.2 V. The electrochemical impedance spectroscopy (EIS) was performed on the same electrochemical workstation with a 10mV amplitude AC signal and a frequency range of 1MHz to 100 mHz. In our lab, we have a set up for monitoring CV and EIS (*Figure 7*).

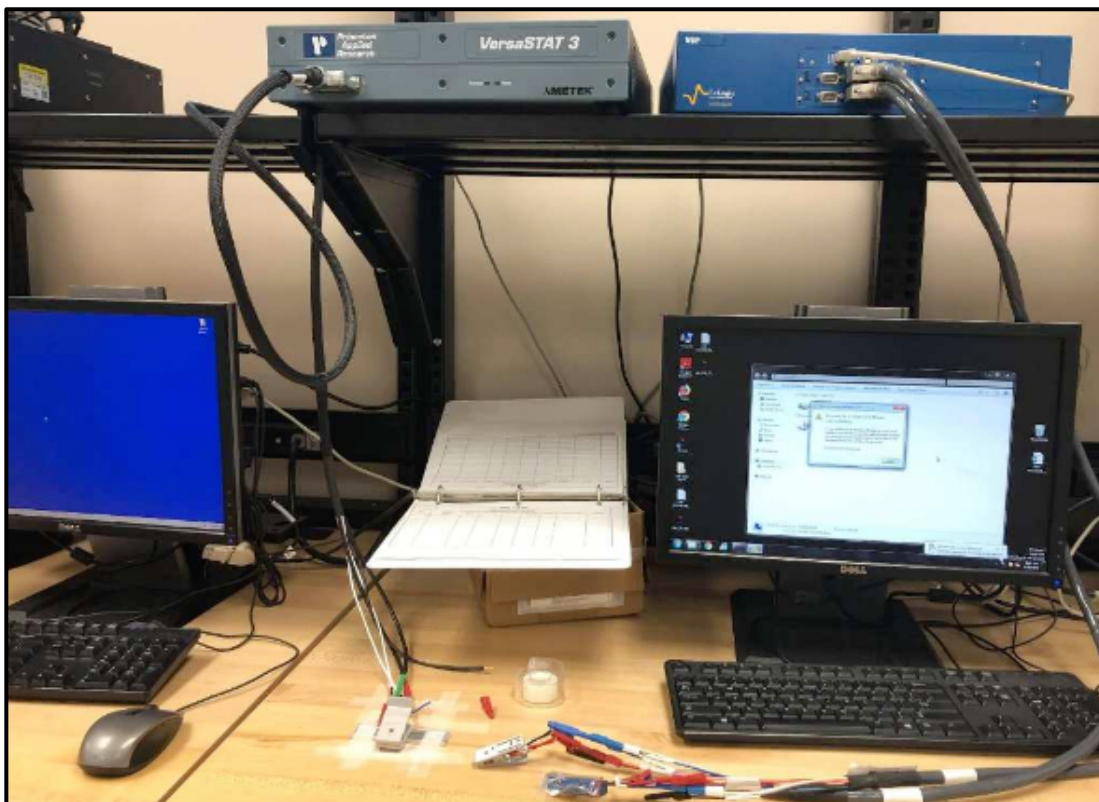


Figure 7: The picture of VERSASTAT and EC-Lab device for measuring CV and EIS

3.6.2 Symmetrical cell and full cell test

Galvanostatic charge-discharge measurements of the coin cells were carried out using the LAND CT2001A system and Neware battery analyzer. *Figure 9* shows the digital photograph of Neware battery analyzer located in DEH 36 at SDSU.



Figure 8: Neware battery analyzer

CHAPTER 4 - RESULTS

4.1 Elastic and electronic properties

As is well recognized, a crucial feature of electrolytes is pure ionic transport with low electrical components. The electrochemical window of a solid electrolyte, which governs the operating voltage range of a battery, is directly dictated by a material's electronic structure [28]. While the SSE should be ionically conductive, but it must be electrically insulating to avoid any internal discharging. Therefore, a wide bandgap material helps to avoid such electrical conduction, even when the SSE heats up after long charge-discharge cycles. *Figure 9(c-d)* shows the atom projected density of states (DOS) and electronic band structure of the cubic double anti-perovskite, $\text{Li}_6\text{OS}(\text{BH}_4)_2$, which indicates that it is insulating to electrons due to the presence of very large forbidden energy gap of 4.027eV between the conduction band minimum (CBM) and valence band maximum (VBM). (*Figure 9b*). Additionally, at the equilibrium lattice constant of 10.0Å, as shown in *Figure 1a*, the bulk-modulus of $\text{Li}_6\text{OS}(\text{BH}_4)_2$ is determined to be 128.5 GPa using the Birch–Murnaghan equation of state [29].

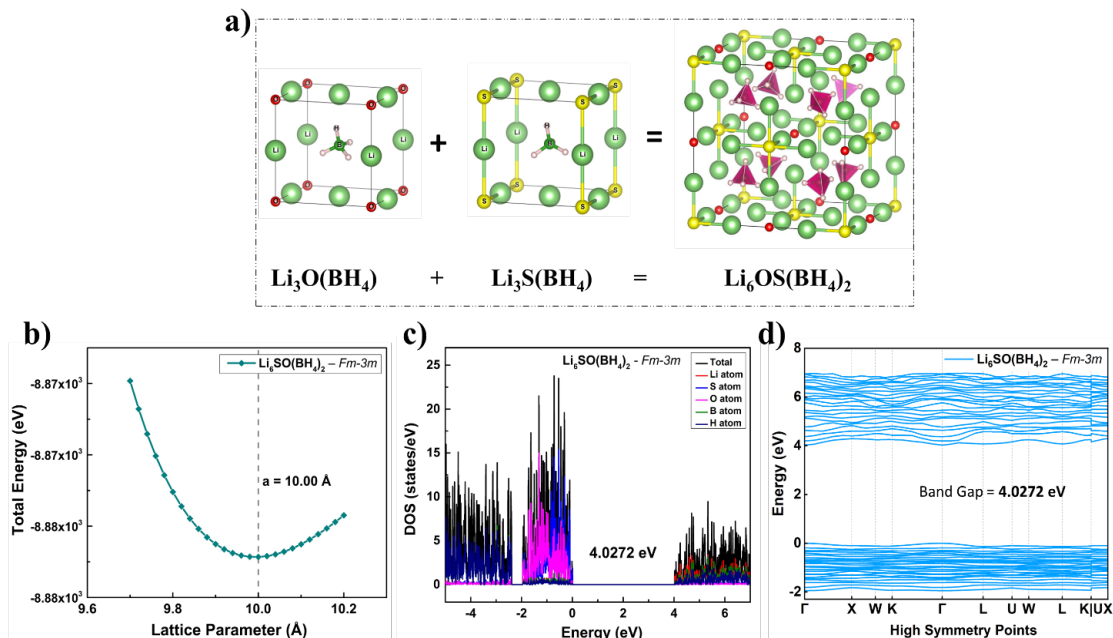


Figure 9: (a) Schematics of the anti-perovskite structures of $\text{Li}_3\text{O}(\text{BH}_4)$ and $\text{Li}_3\text{S}(\text{BH}_4)$, and double anti-perovskite structure of the $\text{Li}_6\text{SO}(\text{BH}_4)_2$; (b) Total energy as a function of relative lattice constant, a (Å); (c) atom projected density of states (DOS), and (d) electronic band structure of $\text{Li}_6\text{SO}(\text{BH}_4)_2$.

These results are computed using PBE0 hybrid functional [30] for improved accuracy of the band structure calculation by accounting for some non-local effect in the exchange-correlation functional.

The electron states of anions dominate this material's VBM and CBM. Additionally, it is demonstrated that the bandgap is mostly influenced by the type of chalcogen species (O, S), with the gap value being related to the total bonding strength. A forbidden gap larger than that of S-based compounds exists in the O-containing substance with the highest degree of covalent bonding.

In our case, we have used superhalogen on the halogen site resulting $\text{Li}_6\text{OS}(\text{BH}_4)_2$, and Table 1 lists the USPEX search results for stable structures with geometrically relaxed lattice parameters for compositions including $\text{Li}_6\text{PSO}_4\text{I}$, $\text{Li}_6\text{PSO}_4\text{I}$, and Li_6OSI_2 , which have thermodynamically favored structures based on the anti-perovskite phase (Pm3m). Thus far, the proposed material not only showed a good and compatible bandgap structure as a double anti-perovskite but also, we have successfully synthesized and got better cyclic performance. It is important to note that full substitution of I with BH_4 in the perovskite phase results in some mild increases in lattice parameters.

	a	b	c(Å)	α	β	$\gamma(^{\circ})$	Sym	Bandgap
$\text{Li}_6\text{OS}(\text{BH}_4)_2$	10.0	10.0	10.0	90	90	90	Fm-3m	4.03 eV
$\text{Li}_6\text{PS}_3\text{I}$	10.31	10.31	10.31	90	90	90	F-43m	3.1 eV
$\text{Li}_6\text{PSO}_4\text{I}$	8.84	8.84	8.84	90	90	90	F-43m	2.9 eV
Li_6OSI_2	8.6	8.6	8.6	90	90	90	Fm-3m	4.5 eV

Table 1 Lattice constants and symmetry (Sym) groups of $\text{Li}_6\text{OS}(\text{BH}_4)_2$, $\text{Li}_6\text{PSO}_4\text{I}$, $\text{Li}_6\text{PSO}_4\text{I}$, and Li_6OSI_2

4.2 Ionic conductivity measurement

With an applied frequency ranging from 100 mHz to 1 MHz, electrochemical impedance spectroscopy (EIS) was used to evaluate ionic conductivity. A Schlumberger Solartron 1260 frequency response analyzer was used to quantify the amplitude of a sinusoidal signal at a resolution of 10 microvolts. The drop-casted samples were vacuum heated to the temperature necessary for each composition.

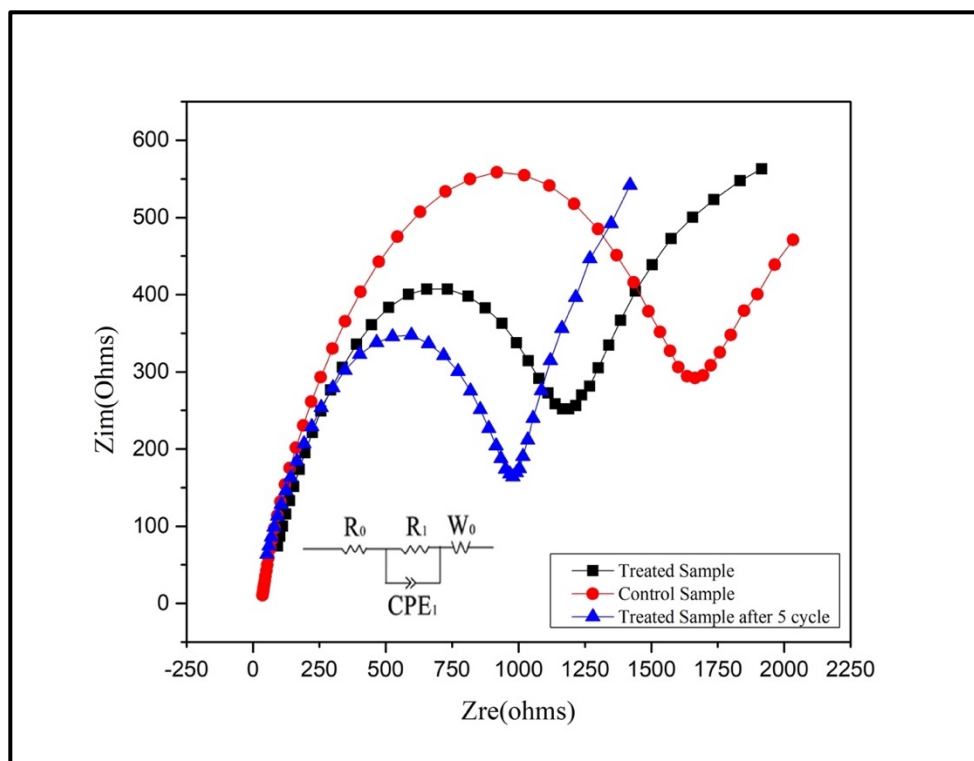


Figure 10: EIS measurement of control and treated samples

The thin film (diameter 15 mm; thickness 200–300 μm) was then placed in a copper clapping assembly within an Argon-filled glovebox to ensure excellent contact with the electrodes and to isolate the sample from the air. The prepared sample was then subjected to any required temperature in a pre-dried testing chamber for 0.5 hours to let the sample temperature settle before performing impedance measurements.

4.3 XRD peaks comparison

The XRD data (*figure 11a*) represents the crystal structure of the solid-state lithium halide, $\text{Li}_6\text{OS}(\text{BH}_4)_2$ electrolyte. The experimental XRD spectrum of the $\text{Li}_6\text{OS}(\text{BH}_4)_2$ fits the simulated spectra with the major peaks corresponding to (011), (002), and (112) Miller indices as well as two smaller peaks with (111) and (022). Additionally, the pattern of

$\text{Li}_6\text{OS}(\text{BH}_4)_2$ agrees with the calculated pattern using lattice parameters from the theoretical work and off-stoichiometric compounds maintained the main characteristics of $\text{Li}_6\text{OS}(\text{BH}_4)_2$. The symmetry of $\text{Li}_6\text{OS}(\text{BH}_4)_2$ is $\text{FM}\bar{3}\text{M}$ (225) with a lattice parameter of 8.578 Å, while that of Li_3OCl is $\text{PM}\bar{3}\text{M}$ (221) with a lattice parameter of 3.910 Å[46].

The structural characteristics of super halogen-based double anti-perovskite phases are included in *Figure 3a*. The $\text{Li}_6\text{OS}(\text{BH}_4)_2$ anti-perovskite mixed phases demonstrate a strong solid solution of two end members. Most samples include minor additional Bragg peaks in their X-ray diffraction pattern, particularly at room temperature. Small tetragonal or orthorhombic aberrations from the ideal cubic structure cause such abnormalities[47]. The reported distortion relates on the pace of sample cooling at the conclusion of the synthesis. At high temperature, many of these minor additional Bragg peaks vanish as the structure (statically or dynamically) becomes closer to the ideal cubic structure.

4.4 Surface topology

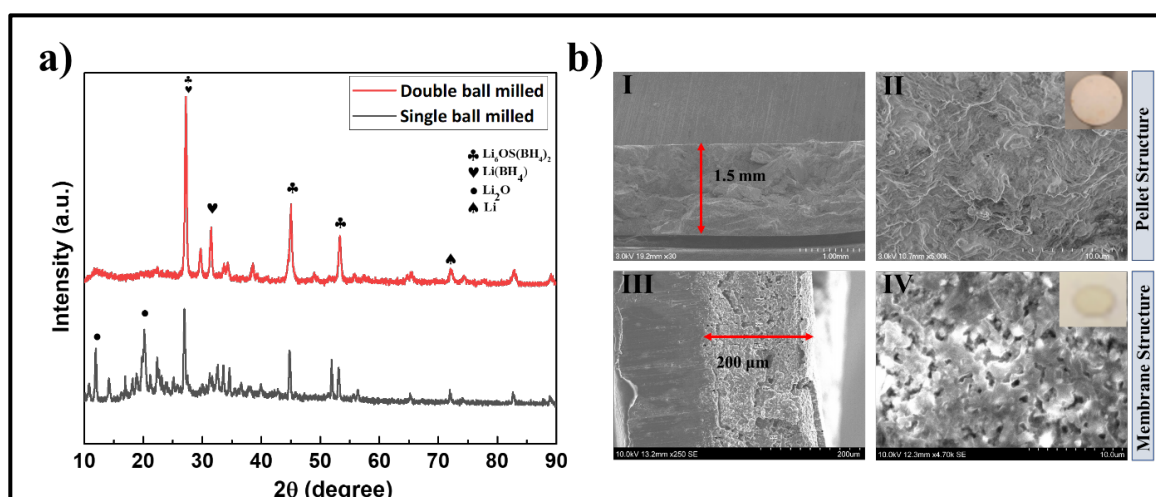


Figure 11: (a) XRD pattern for $\text{Li}_6\text{OS}(\text{BH}_4)_2$ with single (black) and double ball milled (red) sample comparison. (b) morphology and thickness of solid electrolyte as pellet and membrane, exhibiting smooth and integrated morphology

Above figure shows typical morphologies after drop casting. The SEM images of the super halogen-based lithium super halogen electrolyte membrane demonstrate the importance of liquid phase synthesis after melting at $380\text{ }^\circ\text{C}$. The surface of the drop casted electrolyte is uniform with less significant morphological changes across the surface. It appears to be more homogenous with no evidence of crystal formation that could potentially occur without pressure or due to temperature variations because of the complex behavior of viscous liquids close to their glass transition temperatures. Traces of particulate powder features can be observed on the surface of the film. There are both particulate and grain boundaries present in the film, as well as some related porosities.

4.5 Impedance spectroscopy

Figure 10 shows EIS spectra at room temperature 25°C , with insets revealing Each Nyquist plot of an EIS spectrum generally consists of a semicircle and an upward linear tail. The diameter of a semicircle is an electrochemical measure of the space charge area caused by a double layer of polarized charges, resulting in a constant phase element (CPE_1) that is parallelly coupled with a resistance element (R_1) owing to charge transfer difficulties. The charge transfer resistance R_1 term was widely referred to as "grain boundary" resistance in solid electrolytes,[5] [7], particularly those based on the anti-perovskite of Li_3OCl , [27] [28] [29], whereas an ohmic resistor in series (R_0) was generally attributed to transport limited resistance due to "bulk" materials [29] [30] [31]. It should be noted, however, that the presence of a CPE is not always associated with grain boundaries,

as polycrystalline materials with excellent ionic conductivity are free of such a CPE element in equivalent circuits [27], despite grain boundaries being widely recognized as fast diffusion channels in condensed matter. As a result, unless passivated boundary layers are present, there is minimal physical foundation for the formation of considerable "grain boundary" resistance in solid electrolytes.

4.6 Symmetrical cell performance

The cyclability and compatibility of $\text{Li}_6\text{OS}(\text{BH}_4)_2$ film in contact with metallic Li were evaluated using a symmetric cell of $\text{Li}/\text{Li}_6\text{OS}(\text{BH}_4)_2/\text{Li}$ by applying a constant direct-current of $40\mu\text{A}/\text{cm}^2$ with a periodically changing polarity. *Figure 12* shows the voltage profile of the cell cycled continuously for 3000 h (1 h per half a cycle). As shown in *figure 12*, the voltage continues to rise (due to the increase of resistance) throughout cycling testing, particularly during the first few cycles. However, the rate of increase reduces with time, indicating that this system is self-stabilizing. Thus, we hypothesize that there are interactions between Li and $\text{Li}_6\text{OS}(\text{BH}_4)_2$ at their interfaces, which may be induced by the oxidation of Li metal by oxygen from the $\text{Li}_6\text{OS}(\text{BH}_4)_2$ electrolyte or other oxygen sources. However, after a specific amount of cycle tests, the cell might attain a stable condition.

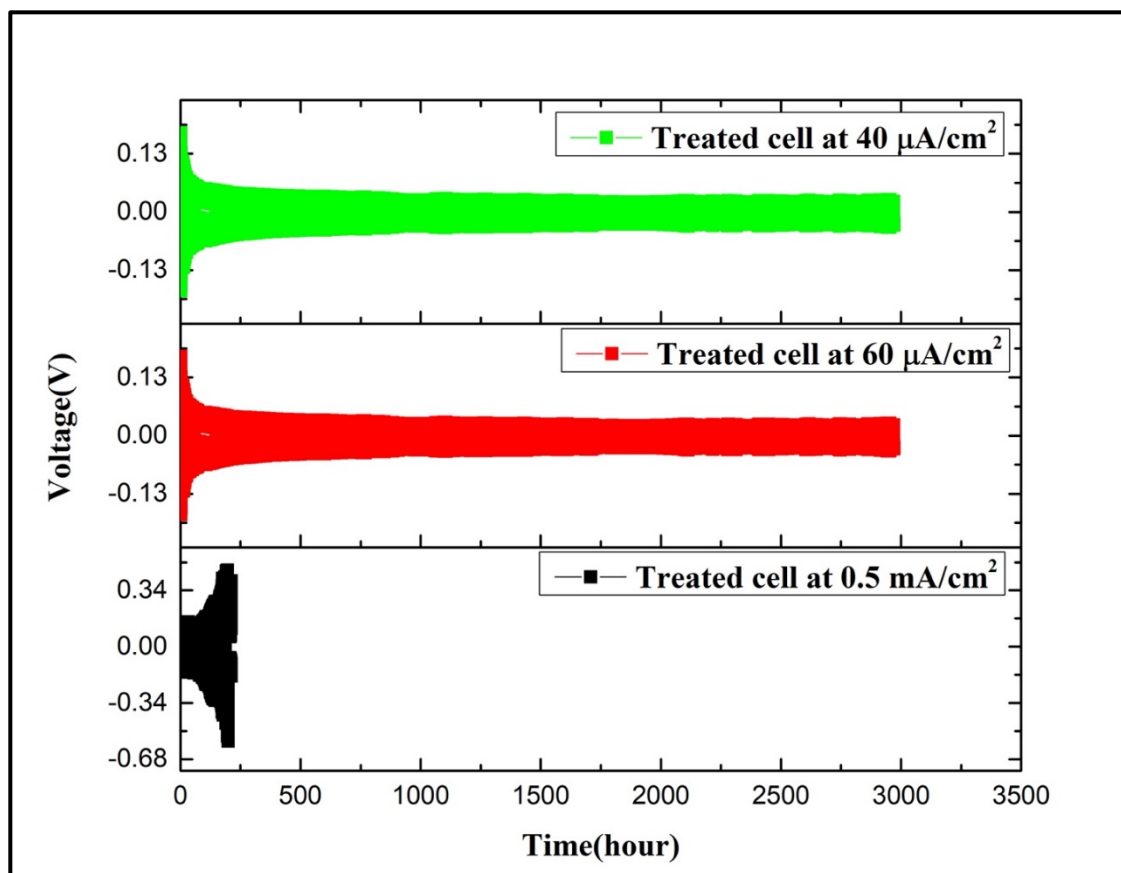


Figure 12: Voltage profile of symmetrical cell at $40\mu\text{A}/\text{cm}^2$, $60\mu\text{A}/\text{cm}^2$ and $0.5\text{ mA}/\text{cm}^2$

4.7 Full cell performance

Figure 13 shows the rate capability test using bare Li and double anti-perovskite coated Li anode coupled with LFP cathode. It can be observed that the double anti-perovskite coated Li/LFP full cell showed a higher capacity at a higher current density rate compared to the bare Li/LFP full cell. At 0.02 C, the double anti-perovskite coated Li/LFP full cell a charge /discharge capacity of $\sim 132/125\text{ mAhg}^{-1}$, and the bare Li/LFP full cell showed $\sim 85/84\text{ mAhg}^{-1}$. The full cell test results are in good agreement with the symmetrical cell test. The synergetic effect of SEI components enhanced electrochemical battery performance.

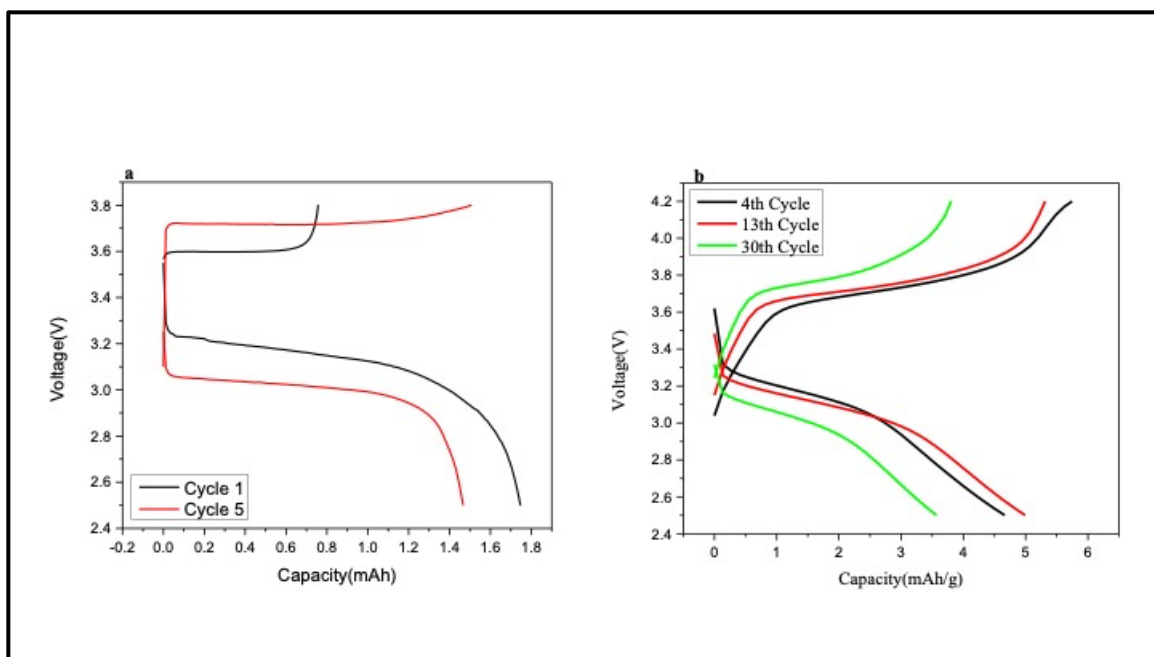


Figure 13: Full cell test (a. Control sample, b. Treated sample)

The control sample was prepared using lithium as anode and LFP as cathode and in between normal separator is used with liquid electrolyte. For the treated one, double anti-perovskite is drop casted in anode side and separator is not used further. Treated sample performed better compared to the controlled one.

CHAPTER 5 - DISCUSSION

5.1 Conclusion

The double anti-perovskite $\text{Li}_6\text{OS}(\text{BH}_4)_2$ compound was successfully synthesized under the direction of previous theoretical work, which anticipated excellent ionic transportation in this novel material system, as well as strong thermodynamic and electrochemical stability. Crystal structure of $\text{Li}_6\text{SO}(\text{BH}_4)_2$ with lowest internal energy is identified, i.e., FCC, which matches with the crystal structure of the component anti-perovskite materials, $\text{Li}_3\text{O}(\text{BH}_4)$ and $\text{Li}_3\text{S}(\text{BH}_4)$. Structural study indicates the SSE is highly stable mechanically, as indicated by its large bulk-modulus. Thus, it will be able to withstand high external or packaging pressure of the battery cell. Study of electronic band structure and Density of States (DOS) indicate that SSE is electrically insulating with large band gap, keeping it safe from any internal electrical discharging. Ion transport study indicates that the SSE has relatively low activation energy barrier for Li-ion migration in the SSE. Both anti-perovskite and double anti-perovskite materials are fundamentally vulnerable to surface reconstruction, resulting in large boundary resistances. The use of amorphous structures is demonstrated to be beneficial in fulfilling the full potential of the novel chemical as a competitive electrolyte solution for solid Li-ion batteries. Using a symmetric Li/ $\text{Li}_6\text{OS}(\text{BH}_4)_2$ /Li cell, the cyclability and compatibility of $\text{Li}_6\text{OS}(\text{BH}_4)_2$ film with Li metal were measured, with the resistance first increasing and then stabilizing at a particular amount. Anti-perovskite $\text{Li}_6\text{OS}(\text{BH}_4)_2$ electrolyte films with increased ionic conductivity show significant potential for battery applications requiring high-level safety and high energy density, such as electric vehicles.

5.2 Future work

The novel material that we used in our project can be further modified to get better full cell performance and has lot of potential to be further used in commercial solid state battery technology. This novel solid electrolyte can be further used with materials having higher theoretical capacity to obtain better ionic conductivity. This will help to improve the reversibility and cycling stability of high-capacity anode materials.

LITERATURE CITED

- [1] T. Famprikis, P. Canepa, J. A. Dawson, M. S. Islam, and C. Masquelier, “Fundamentals of inorganic solid-state electrolytes for batteries,” *Nat. Mater.*, vol. 18, no. 12, Art. no. 12, Dec. 2019, doi: 10.1038/s41563-019-0431-3.
- [2] F. H. Gandoman *et al.*, “Chapter 16 - Reliability evaluation of Li-ion batteries for electric vehicles applications from the thermal perspectives,” in *Uncertainties in Modern Power Systems*, A. F. Zobaa and S. H. E. Abdel Aleem, Eds. Academic Press, 2021, pp. 563–587. doi: 10.1016/B978-0-12-820491-7.00016-5.
- [3] G. Zhang, X. Wei, X. Tang, J. Zhu, S. Chen, and H. Dai, “Internal short circuit mechanisms, experimental approaches and detection methods of lithium-ion batteries for electric vehicles: A review,” *Renew. Sustain. Energy Rev.*, vol. 141, p. 110790, May 2021, doi: 10.1016/j.rser.2021.110790.
- [4] A. Gurung *et al.*, “A review on strategies addressing interface incompatibilities in inorganic all-solid-state lithium batteries,” *Sustain. Energy Fuels*, vol. 3, no. 12, pp. 3279–3309, Nov. 2019, doi: 10.1039/C9SE00549H.
- [5] A. Yoshino, K. Sanechika, and T. Nakajima, “Secondary battery,” US4668595A, May 26, 1987 Accessed: Jan. 04, 2022. [Online]. Available: <https://patents.google.com/patent/US4668595A/en>
- [6] F. Zheng, M. Kotobuki, S. Song, M. O. Lai, and L. Lu, “Review on solid electrolytes for all-solid-state lithium-ion batteries,” *J. Power Sources*, vol. 389, pp. 198–213, Jun. 2018, doi: 10.1016/j.jpowsour.2018.04.022.
- [7] T. P. Kumar, T. S. D. Kumari, and M. A. Stephan, “Carbonaceous anode materials for lithium-ion batteries – the road ahead,” *J. Indian Inst. Sci.*, vol. 89, no. 4, Art. no. 4, 2009.
- [8] “Silicon carbide-free graphene growth on silicon for lithium-ion battery with high volumetric energy density | Nature Communications.” https://www.nature.com/articles/ncomms8393?TB_iframe=true&width=921.6&height=921.6 (accessed Jan. 04, 2022).
- [9] J. Bhattacharya and C. Wolverton, “Relative stability of normal vs. inverse spinel for 3d transition metal oxides as lithium intercalation cathodes,” *Phys. Chem. Chem. Phys.*, vol. 15, no. 17, pp. 6486–6498, Apr. 2013, doi: 10.1039/C3CP50910A.
- [10] R. Moshtev and B. Johnson, “State of the art of commercial Li ion batteries,” *J. Power Sources*, vol. 91, no. 2, pp. 86–91, Dec. 2000, doi: 10.1016/S0378-7753(00)00458-4.
- [11] Q. Zhang, K. Liu, F. Ding, and X. Liu, “Recent advances in solid polymer electrolytes for lithium batteries,” *Nano Res.*, vol. 10, no. 12, pp. 4139–4174, Dec. 2017, doi: 10.1007/s12274-017-1763-4.
- [12] J. Asenbauer, T. Eisenmann, M. Kuenzel, A. Kazzazi, Z. Chen, and D. Bresser, “The success story of graphite as a lithium-ion anode material – fundamentals, remaining challenges, and recent developments including silicon (oxide) composites,” *Sustain. Energy Fuels*, vol. 4, no. 11, pp. 5387–5416, 2020, doi: 10.1039/D0SE00175A.

- [13] C. Yan *et al.*, “4.5 V High-Voltage Rechargeable Batteries Enabled by the Reduction of Polarization on the Lithium Metal Anode,” *Angew. Chem.*, vol. 131, no. 43, pp. 15379–15382, 2019, doi: 10.1002/ange.201908874.
- [14] “Anti-perovskite materials for energy storage batteries - Deng - - InfoMat - Wiley Online Library.” <https://onlinelibrary.wiley.com/doi/full/10.1002/inf2.12252> (accessed Jan. 04, 2022).
- [15] A. Manthiram, X. Yu, and S. Wang, “Lithium battery chemistries enabled by solid-state electrolytes,” *Nat. Rev. Mater.*, vol. 2, no. 4, pp. 1–16, Feb. 2017, doi: 10.1038/natrevmats.2016.103.
- [16] T. Famprikis, P. Canepa, J. A. Dawson, M. S. Islam, and C. Masquelier, “Fundamentals of inorganic solid-state electrolytes for batteries,” *Nat. Mater.*, vol. 18, no. 12, pp. 1278–1291, Dec. 2019, doi: 10.1038/s41563-019-0431-3.
- [17] J. C. Bachman *et al.*, “Inorganic Solid-State Electrolytes for Lithium Batteries: Mechanisms and Properties Governing Ion Conduction,” *Chem. Rev.*, vol. 116, no. 1, pp. 140–162, Jan. 2016, doi: 10.1021/acs.chemrev.5b00563.
- [18] “New horizons for inorganic solid state ion conductors - Energy & Environmental Science (RSC Publishing) DOI:10.1039/C8EE01053F.” <https://pubs.rsc.org/en/content/articlehtml/2018/ee/c8ee01053f> (accessed Jan. 04, 2022).
- [19] X. Yao *et al.*, “All-solid-state lithium batteries with inorganic solid electrolytes: Review of fundamental science,” *Chin. Phys. B*, vol. 25, no. 1, p. 018802, Jan. 2016, doi: 10.1088/1674-1056/25/1/018802.
- [20] N. Kamaya *et al.*, “A lithium superionic conductor,” *Nat. Mater.*, vol. 10, no. 9, Art. no. 9, Sep. 2011, doi: 10.1038/nmat3066.
- [21] “Tetragonal Li₁₀GeP₂S₁₂ and Li₇GePS₈ – exploring the Li ion dynamics in LGPS Li electrolytes - Energy & Environmental Science (RSC Publishing).” <https://pubs.rsc.org/en/content/articlelanding/2013/ee/c3ee41728j/unauth> (accessed Mar. 19, 2022).
- [22] “High-power all-solid-state batteries using sulfide superionic conductors | Nature Energy.” <https://www.nature.com/articles/nenergy201630> (accessed Mar. 19, 2022).
- [23] X. Xu, Z. Wen, J. Wu, and X. Yang, “Preparation and electrical properties of NASICON-type structured Li_{1.4}Al_{0.4}Ti_{1.6}(PO₄)₃ glass-ceramics by the citric acid-assisted sol-gel method,” *Solid State Ion.*, vol. 178, no. 1–2, pp. 29–34, Jan. 2007, doi: 10.1016/j.ssi.2006.11.009.
- [24] H. Morimoto *et al.*, “Preparation of lithium ion conducting solid electrolyte of NASICON-type Li_{1+x}Al_xTi_{2-x}(PO₄)₃ (x = 0.3) obtained by using the mechanochemical method and its application as surface modification materials of LiCoO₂ cathode for lithium cell,” *J. Power Sources*, vol. 240, pp. 636–643, Oct. 2013, doi: 10.1016/j.jpowsour.2013.05.039.
- [25] R. Kanno and M. Murayama, “Lithium Ionic Conductor Thio-LISICON: The Li₂S-GeS₂-P₂S₅ System,” *J. Electrochem. Soc.*, vol. 148, no. 7, p. A742, 2001, doi: 10.1149/1.1379028.
- [26] P. Raghavan *et al.*, “Solid-State Electrolytes for Lithium-Ion Batteries: Novel Lithium-Ion Conducting Ceramic Materials: Oxides (Perovskite, Anti-Perovskite) and Sulfide-Type Ion Conductors,” in *Ceramic and Specialty Electrolytes for Energy Storage Devices*, CRC Press, 2021.

- [27] V. Thangadurai and W. Weppner, "Recent progress in solid oxide and lithium ion conducting electrolytes research," *Ionics*, vol. 12, no. 1, pp. 81–92, May 2006, doi: 10.1007/s11581-006-0013-7.
- [28] H. Muramatsu, A. Hayashi, T. Ohtomo, S. Hama, and M. Tatsumisago, "Structural change of Li₂S–P₂S₅ sulfide solid electrolytes in the atmosphere," *Solid State Ion.*, vol. 182, no. 1, pp. 116–119, Feb. 2011, doi: 10.1016/j.ssi.2010.10.013.
- [29] M. M. Kabir and D. E. Demirocak, "Degradation mechanisms in Li-ion batteries: a state-of-the-art review," *Int. J. Energy Res.*, vol. 41, no. 14, pp. 1963–1986, 2017, doi: 10.1002/er.3762.
- [30] "A Review of Li-ion Battery Equivalent Circuit Models -Transactions on Electrical and Electronic Materials | Korea Science." <https://www.koreascience.or.kr/article/JAKO201607365702136.page> (accessed Jun. 18, 2022).
- [31] J. Epp, "4 - X-ray diffraction (XRD) techniques for materials characterization," in *Materials Characterization Using Nondestructive Evaluation (NDE) Methods*, G. Hübschen, I. Altpeter, R. Tschuncky, and H.-G. Herrmann, Eds. Woodhead Publishing, 2016, pp. 81–124. doi: 10.1016/B978-0-08-100040-3.00004-3.
- [32] D. L. Bish and J. E. Post, *Modern Powder Diffraction*. Walter de Gruyter GmbH & Co KG, 2018.
- [33] "X-ray diffraction and the identification and analysis of clay minerals." <https://www.cabdirect.org/cabdirect/abstract/19901943215?freeview=true> (accessed Jun. 18, 2022).
- [34] V.-D. Hodoroba, "Chapter 4.4 - Energy-dispersive X-ray spectroscopy (EDS)," in *Characterization of Nanoparticles*, V.-D. Hodoroba, W. E. S. Unger, and A. G. Shard, Eds. Elsevier, 2020, pp. 397–417. doi: 10.1016/B978-0-12-814182-3.00021-3.
- [35] P. D. Ngo, "Energy Dispersive Spectroscopy," in *Failure Analysis of Integrated Circuits: Tools and Techniques*, L. C. Wagner, Ed. Boston, MA: Springer US, 1999, pp. 205–215. doi: 10.1007/978-1-4615-4919-2_12.
- [36] P. T. Kissinger and W. R. Heineman, "Cyclic voltammetry," *J. Chem. Educ.*, vol. 60, no. 9, p. 702, Sep. 1983, doi: 10.1021/ed060p702.
- [37] "pdf.pdf." Accessed: Jun. 18, 2022. [Online]. Available: <https://iopscience.iop.org/article/10.1149/2.20192if/pdf#page=50>
- [38] F. Ciucci, "Modeling electrochemical impedance spectroscopy," *Curr. Opin. Electrochem.*, vol. 13, pp. 132–139, Feb. 2019, doi: 10.1016/j.coelec.2018.12.003.
- [39] "QUANTUM ESPRESSO: a modular and open-source software project for quantum simulations of materials - IOPscience." <https://iopscience.iop.org/article/10.1088/0953-8984/21/39/395502/meta> (accessed May 09, 2022).
- [40] "Phys. Rev. B 88, 085117 (2013) - Optimized norm-conserving Vanderbilt pseudopotentials." <https://journals.aps.org/prb/abstract/10.1103/PhysRevB.88.085117> (accessed May 09, 2022).
- [41] "Phys. Rev. Lett. 77, 3865 (1996) - Generalized Gradient Approximation Made Simple." <https://journals.aps.org/prl/abstract/10.1103/PhysRevLett.77.3865> (accessed May 09, 2022).

- [42] H. J. Monkhorst and J. D. Pack, "Special points for Brillouin-zone integrations," *Phys. Rev. B*, vol. 13, no. 12, pp. 5188–5192, Jun. 1976, doi: 10.1103/PhysRevB.13.5188.
- [43] S. Wu, Z. Dong, P. Wu, and F. Boey, "Effect of transition metal (M = Co, Ni, Cu) substitution on electronic structure and vacancy formation of Li₃N," *J. Mater. Chem.*, vol. 21, no. 1, pp. 165–170, 2011, doi: 10.1039/C0JM01883J.
- [44] Z. Wang, H. Xu, M. Xuan, and G. Shao, "From anti-perovskite to double anti-perovskite: tuning lattice chemistry to achieve super-fast Li⁺ transport in cubic solid lithium halogen–chalcogenides," *J. Mater. Chem. A*, vol. 6, no. 1, pp. 73–83, 2018, doi: 10.1039/C7TA08698A.
- [45] K. Momma and F. Izumi, "VESTA 3 for three-dimensional visualization of crystal, volumetric and morphology data," *J. Appl. Crystallogr.*, vol. 44, no. 6, Art. no. 6, Dec. 2011, doi: 10.1107/S0021889811038970.
- [46] "Lithium Ion Conductivity in Double Antiperovskite Li_{6.5}OS_{1.5}I_{1.5}: Alloying and Boundary Effects | ACS Applied Energy Materials." <https://pubs.acs.org/doi/abs/10.1021/acsaem.9b00861> (accessed Mar. 19, 2022).
- [47] Y. Zhao and L. L. Daemen, "Superionic Conductivity in Lithium-Rich Anti-Perovskites," *J. Am. Chem. Soc.*, vol. 134, no. 36, pp. 15042–15047, Sep. 2012, doi: 10.1021/ja305709z.